

Spectral Energy Distributions of Type 1 AGN in XMM-COSMOS Survey II - Shape Evolution

Heng Hao^{1,2*}, Martin Elvis¹, Francesca Civano¹, Gianni Zamorani³, Luis C. Ho⁴, Andrea Comastri³, Angela Bongiorno^{5,6}, Andrea Merloni⁵, Marcella Brusa⁵, Jonathan R. Trump⁷, Mara Salvato^{8,9}, Chris D. Impey¹⁰, Anton M. Koekemoer¹¹, Giorgio Lanzuisi⁵, Annalisa Celotti^{2,12}, Knud Jahnke¹³, Cristian Vignali^{3,14}, John D. Silverman¹⁵, C. Megan Urry¹⁶, Kevin Schawinski¹⁷, Peter Capak¹⁸

¹Harvard-Smithsonian Center for Astrophysics, 60 Garden Street, Cambridge, MA 02138, USA

²SISSA, Via Bonomea 265, I-34136 Trieste, Italy

³INAF-Osservatorio Astronomico di Bologna, via Ranzani 1, I-40127 Bologna, Italy

⁴The Observatories of the Carnegie Institute for Science, Santa Barbara Street, Pasadena, CA 91101, USA

⁵Max Planck Institute für Extraterrestrische Physik, Postfach 1312, 85741, Garching bei München, Germany

⁶INAF-Osservatorio Astronomico di Roma, Via di Frascati 33, 00040, Monteporzio Catone, Rome, Italy

⁷UCO/Lick Observatory, University of California, Santa Cruz, CA 95064, USA

⁸IPP - Max-Planck-Institute for Plasma Physics, Boltzmann Strasse 2, D-85748, Garching bei München, Germany

⁹Excellence Cluster, Boltzmann Strasse 2, D-85748, Garching bei München, Germany

¹⁰Steward Observatory, University of Arizona, 933 North Cherry Avenue, Tucson, AZ 85721, USA

¹¹Space Telescope Science Institute, 3700 San Martin Drive, Baltimore, MD 21218, USA

¹²INAF - Osservatorio Astronomico di Brera, via E. Bianchi 46, I-23807 Merate, Italy

¹³Max-Planck-Institut für Astronomie, Königstuhl 17, Heidelberg, D-69117, Germany

¹⁴Dipartimento di Astronomia, Università degli Studi di Bologna, Via Ranzani 1, 40127 Bologna, Italy

¹⁵Institute for the Physics and Mathematics of the Universe (IPMU), University of Tokyo, Kashiwanoha 5-1-5, Kashiwa-shi, Chiba 277-8568, Japan

¹⁶Physics Department and Yale Center for Astronomy and Astrophysics, Yale University, New Haven, CT 06511, USA

¹⁷Institute for Astronomy, Department of Physics, ETH Zurich, Wolfgang-Pauli-Strasse 16, CH-8093 Zurich, Switzerland

¹⁸California Institute of Technology, MC 105-24, 1200 East California Boulevard, Pasadena, CA 91125, USA

Version Oct 8th, 2012.

ABSTRACT

The near-infrared to optical-ultraviolet ($0.1 - 10 \mu\text{m}$) spectral energy distribution (SED) shapes of 407 X-ray-selected radio-quiet type 1 AGN in the wide-field “Cosmic Evolution Survey” (COSMOS) have been studied for signs of evolution. For a subsample of 200 radio-quiet quasars with black hole mass estimation and host galaxy correction, we study the mean SEDs as a function of a broad range of redshift, bolometric luminosity, black hole mass and Eddington ratio, and compare them with the Elvis et al. (1994, E94) type 1 AGN mean SED. The mean SEDs in each bin are very similar to each other, showing no evidence of dependence on any of the analyzed parameters. We also checked the SED dispersion as a function of these four parameters, and found no significant dependence. The dispersion of the XMM-COSMOS SEDs is generally larger than E94 SED dispersion in the ultraviolet, which might be largely due to the broader “window function” for COSMOS quasars, and the X-ray based selection technique.

Key words: galaxies: evolution; quasars: general; surveys

1 INTRODUCTION

The nature of the continuum emission of Active Galactic Nuclei (AGN) remains unsettled after several decades of study. Yet, understanding the continuum emission of AGN, from X-rays to radio, is essential to understand the physics

* E-mail: henghao@post.harvard.edu

of accretion onto super massive black holes (SMBHs). The continuum in each spectral region can be ascribed to distinct energy generation mechanisms: jets in the radio (see e.g. the review by Harris & Krawczynski 2006), dust in the infrared (IR, McAlary & Rieke 1988; Sanders et al. 1989), accretion disks in the optical-ultraviolet (UV) and soft X-rays (Shakura & Sunyaev 1973; Rees 1984; Czerny & Elvis 1987), and Compton up-scattering by hot coronae in the hard X-rays (e.g., Zamorani et al. 1981; Laor et al. 1990; Haardt & Maraschi 1991; Williams et al. 1992; Zdziarski et al. 2000; Kawaguchi et al. 2001; Mateos et al. 2005; Mainieri et al. 2007).

Continuum changes with redshift, luminosity or Eddington ratio might be expected. Most SMBH growth occurs during the active ‘AGN’ phases (the ‘Soltan argument’, Soltan 1982), implying that most bulges went through an AGN phase (e.g. Magorrian et al. 1998). Rapid growth of central SMBHs happens in high-redshift and high-luminosity quasars emitting near the Eddington limit (Barth et al. 2003; Vestergaard 2004; Jiang et al. 2006; Kurk et al. 2007; but see also Steinhardt & Elvis 2010). The space density of X-ray-selected, highly luminous AGN peaks at around $z = 2.5$, and declines at $z > 3$ (Silverman et al. 2005, Brusa et al. 2009, Civano et al. 2011). Low-luminosity AGN are more prevalent at $z < 1$ than higher luminosity ones (Cowie et al. 2003; Fiore et al. 2003; Ueda et al. 2003; Silverman et al. 2005). As the central SMBH is the driver of the emission, one might expect the quasar SED to evolve as the black hole grows due to accretion.

Many parameters – the black hole mass, the AGN luminosity relative to the host galaxy, the accretion rate, the physical properties of the accretion disk and the properties of the absorbing dust – might affect the shape of the AGN SED (Wilkes 2003). For instance, the optical to X-ray spectral index $[\alpha_{OX} = 0.384 \log(F_{2\text{keV}}/F_{2500\text{\AA}})]$, correlates with luminosity but not with redshift (e.g. Vignali et al. 2003a; Steffen et al. 2006; Just et al. 2007; Young et al. 2010; Lusso et al. 2010). It is possible that similar dependency of luminosity in the SED shape exists at other wavelengths.

Observations indicate a tight link between SMBH growth and galaxy evolution (e.g. Magorrian et al. 1998; Marconi & Hunt 2003; Tremaine et al. 2002; Menci et al. 2008). Locally, SMBHs appear to reside at the center of most galaxies and the SMBH masses are tightly correlated with their masses (e.g. Kormendy & Richstone 1995; Marconi & Hunt 2003) and velocity dispersions (i.e. $M_{BH} - \sigma$ relations; Ferrarese & Merrit 2000; Gebhardt et al. 2000; Tremaine et al. 2002). Some evidence for evolution of this relationship has been reported using several methods (e.g. Peng et al. 2006; Shields et al. 2006; Ho 2007; Merloni et al. 2010). This evolution would imply that the feedback of the SMBH to the host galaxy evolves. Similar evolution in the innermost regions (within the ‘torus’) is possible too. All of these processes could lead to different SED shapes.

However, no evolution of the AGN SED has yet been demonstrated. There is no convincing evidence for any change of SED with redshift (Silverman et al. 2002; Mathur et al. 2002; Brandt et al. 2002; Vignali et al. 2003b). High redshift quasars (up to redshift 7) show optical spectra similar to low redshift quasars from the SDSS (Jiang et al. 2007, Mortlock et al. 2011). There is evidence, though, that the SEDs of extremely low-luminosity ($L_{bol} \lesssim 10^{42} \text{ erg/s}$) nu-

clei are remarkably different from those of luminous ($L_{bol} \gtrsim 10^{44} \text{ erg/s}$) AGN (Ho 1999, Ho 2008).

So far, the systematic study of the dependency of the SED shape with physical parameters has been limited by difficulty in obtaining a large sample size with good multi-wavelength coverage. The Cosmological Evolution Survey (COSMOS, Scoville et al. 2007) has the appropriate combination of depth, area and extensive multi-wavelength data that allows for a sensitive survey of AGN to address this question.

The COSMOS field has been imaged with XMM-Newton for a total of ~ 1.5 Ms (Hasinger et al. 2007; Cappelluti et al. 2007, 2009). Optical identifications were made by Brusa et al. (2010) for the entire XMM-COSMOS sample. Photometric properties and redshifts were produced for each point source. This extensive data set allows us to make a systematic study of the evolution of the SED shape, which is the main purpose of this paper.

From this complete sample, we extracted a sample of 413 type 1 AGN (broad emission line FWHM $> 2000 \text{ km s}^{-1}$). The type 1 AGN SED sample catalog is described in detail in Elvis et al. (2012, hereafter Paper I). It includes quasars with redshifts $0.1 \leq z \leq 4.3$ and magnitudes $16.9 \leq i_{AB} \leq 24.8$, with 98% of the sources being radio-quiet (Hao et al. 2012a). This sample is twenty times larger than the Elvis et al. (1994, E94 hereafter) radio-quiet type 1 AGN SED sample, and has full wavelength coverage from radio to X-rays (for a total of 43 photometric bands, Paper I) and high confidence level spectroscopic redshifts (Trump et al. 2009a; Schneider et al. 2007; Lilly et al. 2007, 2009). The mean SED of the XMM-COSMOS type 1 AGN was calculated and compared to previous studies: E94, Richards et al. (2006), Hopkins et al. (2007) and Shang et al. (2011) in paper I. We found that in the near-IR to optical-UV bands, the previous studies have very similar shapes, while the XMM-COSMOS mean host-corrected quasar SED has a less prominent ‘big-blue bump’, due to possible excess host contribution, not corrected because of the dispersion in the black hole mass and host luminosity scaling relationship itself. In this paper, we compare the Paper I sample with E94 as a representative.

Paper I presented the selection and properties of the XMM-COSMOS type 1 AGN sample of 413 quasars (XC413 hereinafter). We used seven radio-loud criteria ($R_L = \log(f_{5\text{GHz}}/f_B) > 1$, Wilkes & Elvis 1987; $q_{24} = \log(f_{24\mu\text{m}}/f_{1.4\text{GHz}}) < 0$, Appleton et al. 2004; $R_{uv} = \log(f_{5\text{GHz}}/f_{2500\text{\AA}}) > 1$, Stocke et al. 1992; $P_{5\text{GHz}} = \log[P_{5\text{GHz}}(W/H_z/Sr)] > 24$, Goldschmidt et al. 1999; and $R_X = \log(\nu L_\nu(5\text{GHz})/L_X) > -3$, Terashima & Wilson 2003) to define a radio-loud quasar. We find that the radio-loud fraction is 1.5%–4.5% using any criterion, except R_{uv} , which is subject to the reddening and host contamination issues (Hao et al. 2012a). Using two criteria at the same time, the radio-loud fraction is $\lesssim 8/413 = 2\%$. Only 6 XC413 quasars satisfy all the seven criteria. We define these 6 quasars in this catalog as radio-loud (Paper I; Hao et al. 2012a). We refer to the radio-quiet XC413 as XCRQ407 hereinafter.

Estimates of black hole mass (M_{BH}) for 206 of XC413 have been made by Merloni et al. (2010) and Trump et al. (2009b). Both papers used single-epoch spectra and applied the scaling relations from reverberation mapping of Vestergaard & Peterson (2006). This method requires a high S/N

Table 1. Source Properties in Parameter Space¹

XID	z ^a	log M _{BH} ^b [M _⊙]	log L _{bol} ^c [erg s ⁻¹]	log λ _E ^d	log L _{all} ^e [erg s ⁻¹]	L _{ir} /L _{bol} ^f %	L _{opt} /L _{bol} ^g %	L _X /L _{bol} ^h %	log L _{bol,hc} ⁱ [erg s ⁻¹]
1	0.373	8.58	45.45	-1.22	45.46	19.7	38.2	5.8	...
2	1.024	8.96	46.02	-1.04	46.09	38.2	20.9	32.4	46.00
3	0.345	8.66	45.37	-1.39	45.39	35.6	25.4	18.2	45.28
4	0.132	7.31	44.50	-0.91	44.55	45.7	39.7	3.4	44.43
5	1.157	...	46.16	...	46.21	38.5	28.5	14.5	...
6	0.360	8.64	45.10	-1.64	45.20	39.2	43.7	6.0	44.91
7	0.519	8.38	45.42	-1.06	45.44	39.5	28.9	18.8	45.37
8	0.699	7.96	45.96	-0.11	45.97	34.1	33.1	7.5	45.96
9	1.459	8.86	46.19	-0.77	46.28	48.9	22.4	14.3	46.18
...

¹ A portion of the table is shown here for guidance. The complete table will be available online.

^a The spectroscopic redshifts are from Trump et al. (2009a), Schneider et al. (2007), Lilly et al. (2007, 2009)

^b The black hole mass estimates are from Trump et al. (2009b) and Merloni et al. (2010)

^c Calculated by integrating the rest frame SED from 24 μm to 40 keV.

^d λ_E = L_{bol}/L_{Edd}, details in § 2.3.

^e Calculated by integrating the rest frame SED from 1.4 GHz to 40 keV.

^f L_{ir} is calculated by integrating the rest frame SED from 24 μm to 1 μm.

^g L_{opt} is calculated by integrating the rest frame SED from 1 μm to 912 Å.

^h L_X is calculated by integrating the rest frame SED from 0.5 keV to 40 keV.

ⁱ Calculated by integrating the rest frame host-corrected SED from 24 μm to 40 keV for 203 quasars in the XMM-COSMOS sample.

spectrum with the broad emission line not near the ends of the spectra. For the quasars with only zCOSMOS spectra, the black hole mass was estimated only for those with MgII lines in the spectra (Merloni et al. 2010), using the calibration of McLure & Jarvis (2002). 206 quasars out of XC413, that is 203 quasars out of XCRQ407 have black hole mass estimates. Paper I estimated the host galaxy contribution for 203 of these 206 quasars using the scaling relationship between black hole mass and host luminosity (Marconi & Hunt 2003) adding an evolutionary term (Bennert et al. 2010, 2011), excluding the 3 which had over-subtraction problems (the estimated host galaxy luminosity is larger than the observed luminosity). We define this sub-sample (SS) as SS203. In SS203, 200 quasars are radio-quiet. We refer to this sub-sample as SSRQ200.

In Paper I, rest frame SEDs of XC413 were constructed on a uniform frequency grid ($\Delta \log \nu = 0.02$) from radio to X-rays. As there is limited data in the far-IR ($> 10 \mu\text{m}$ in rest frame) and longer wavelengths, and because the UV flux is strongly affected by both variability and strong broad emission lines, we defer the analysis of these regions to a later paper. In this paper, we focus on the SED shape in the optical to near-IR range, while all the plots are shown in the rest frame 0.1 – 10 μm range. Note that all the sources discussed in this paper are broad line AGN with typical luminosity ($\sim 10^{44} - 10^{47}$ erg/s), typical black hole mass ($\sim 10^7 - 10^9 M_{\odot}$) and typical accretion rates (Eddington ratio larger than 0.01, see in § 2.3).

All the wavelengths discussed in this paper are in the rest frame. We adopt the WMAP 5-year cosmology (Komatsu et al. 2009), with $H_0 = 71 \text{ km s}^{-1} \text{ Mpc}^{-1}$, $\Omega_M = 0.26$ and $\Omega_{\Lambda} = 0.74$.

Table 2. Parameter Range

Parameter	XCRQ407			SSRQ200		
	min	med	max	min	med	max
z	0.10	1.57	4.26	0.13	1.50	4.26
log(M _{BH} /M _⊙)	7.18	8.39	9.34
log L _{all}	44.29	45.71	47.40	44.55	45.77	47.40
log L _{bol}	44.26	45.69	47.28	44.50	45.74	47.28
L _{ir} /L _{bol}	12.8%	35.1%	82.5%	12.8%	35.6%	82.5%
L _{opt} /L _{bol}	9.3%	33.3%	61.1%	9.3%	33.3%	59.7%
L _X /L _{bol}	0.34%	8.6%	45.0%	0.48%	8.4%	45.0%
log λ _E	-1.76	-0.72	0.63

2 PARAMETER SPACE

2.1 Bolometric Luminosity

The bolometric luminosity is the total energy radiated by the quasar at all wavelengths. This luminosity is, in principle, simply calculated by directly integrating the rest-frame SED over the whole wavelength range. In practice, this is difficult and observationally expensive. For the sample discussed in this paper, it is possible to approximate the bolometric luminosity with the SEDs available (Paper I).

As described in Paper I, the SEDs are produced by linearly interpolating between the data points in $\log \nu L_{\nu}$ versus $\log \nu$ space (i.e. connecting the individual points with power laws in linear space). The COSMOS photometry for the XC413 sample is >90% complete from u (CFHT) to MIPS 24 μm, that is over the 1.8 dex wide $0.35 \mu\text{m} - 24 \mu\text{m}$ ($\sim 0.14 \mu\text{m} - 10 \mu\text{m}$ for the typical $z = 1.5$ of XC413) observed frame interpolation is unproblematic (Paper I). In the mid-infrared range, for quasars with 70 μm or 160 μm

detections, we joined the $24\mu\text{m}$ data to the longer wavelength points with a power-law in $\log \nu f_\nu$ vs. $\log \nu$ space; for the others we extrapolated from the rest frame $24\mu\text{m}$ to $8\mu\text{m}$ slope and checked that the extrapolation generally works. As the far-IR to radio photometry data are sparse, for each source with a $> 3\sigma$ VLA detection, we assumed a power law $f_\nu \propto \nu^{-0.5}$ (e.g., Ivezić 2004) in the rest frame 1.4 GHz (21 cm) to 100 GHz (3 mm) range. In the 100 GHz (3 mm) to $160\mu\text{m}$ part, the SED can be approximated by the red end of the grey body $f_\nu \propto \nu^{3+\beta}/(e^{h\nu/kT} - 1)$, when $h\nu \ll kT$, $f_\nu \propto \nu^{2+\beta}$ (e.g. Lapi et al. 2011). The β value is generally chosen in the range 1–2 (Dunne & Eales 2001). We thus choose $\beta = 1$, i.e. we assume a power-law $f_\nu \propto \nu^3$ in this wavelength range. We directly linearly interpolate from Lyman break (1216\AA) and 0.5 keV SED (Laor et al. 1997) in $\log \nu L_\nu$ versus $\log \nu$ space. In the X-rays, we use the measured photon spectral index (Γ , $f_\nu \propto \nu^{(1-\Gamma)}$, Mainieri et al. 2007) and the observed 2 keV luminosity to get the SED in the 0.5 keV–40 keV (rest-frame), which is the range we could have XMM data for XC413.

We used the SEDs from Paper I to calculate two approximations to the bolometric luminosities by integrating the rest frame SED over several different wavelength ranges: (1) from $24\mu\text{m}$ to 40 keV, the range over which COSMOS coverage is virtually complete, as L_{bol} and (2) from 21 cm/1.4 GHz to 40 keV as L_{all} . L_{all} was integrated over all the wavelengths for which we could have data.

As the great majority of the XC413 quasars are radio-quiet and the photometric coverage from $24\mu\text{m}$ to 1.4 GHz is currently sparse (Paper I), we use L_{bol} to avoid unwarranted extrapolation. The contribution of the radio emission to the bolometric luminosity is less than 3% even for the radio-loud sources. Most of the far-IR (at $\gtrsim 100\mu\text{m}$) luminosity is probably due to star-forming activity not the AGN (Netzer et al. 2007, Mullaney et al. 2012; but see Ho 2005). Hence L_{bol} is a good approximation of the true bolometric quasar luminosity defined over the entire wavelength range.

We note that the L_{bol} calculated by directly integrating the SED in the rest frame from IR to X-rays overestimates the quasar emission for two reasons: (1) the contribution from the host galaxy is not excluded; (2) different wavelength ranges of the SED have different emission origins. From the optical short-ward the primary emission is from the innermost region of the quasar (SMBH and accretion disk). The near and mid-IR continuum is the result of reprocessing shorter wavelength radiation of the quasar by dust (Sanders et al. 1989; Suganuma et al. 2006). The reprocessed dust emission thereby includes reprocessed primary radiation emitted in directions different from our line-of-sight. In a non-spherical geometry, as is likely present in quasars, this makes us count more radiation that we would in a 4π averaged calculation. In this sense, we are double-counting the primary emission (e.g. Lusso et al. 2010).

In practice, we do not have good estimates of the host contribution. For SSRQ200, we calculated the bolometric luminosity by integrating the host corrected SED from $24\mu\text{m}$ to 40 keV as $L_{bol, hc}$ (last column in Table 1). As discussed in Paper I, we applied the scaling relationship between black hole mass and host luminosity reported in Marconi & Hunt (2003), and added an evolutionary term (Bennert et al. 2010, 2011), to estimate the contribution of host galaxy.

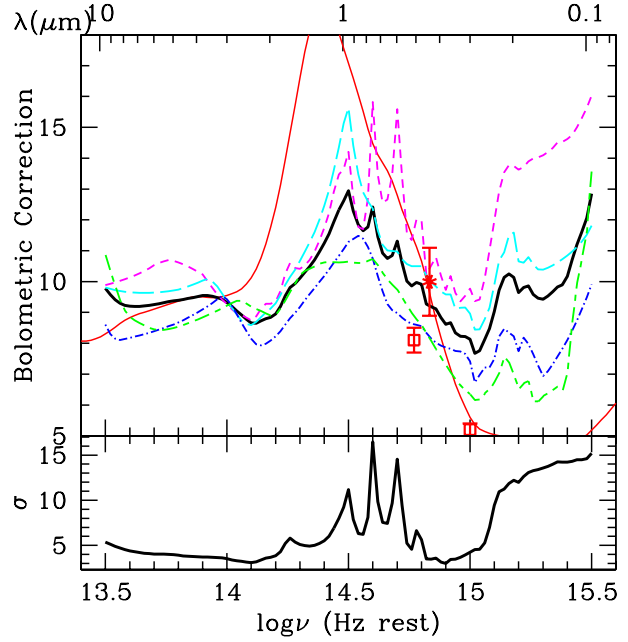


Figure 1. The frequency dependent bolometric correction for the SSRQ200 sample (black solid). The bolometric corrections in different redshift bins are also shown in the same plot (redshift: 0.1–1.2= magenta short dashed line, 50 quasars; 1.2–1.5= cyan long dashed line, 50 quasars; 1.5–1.8= blue dot dashed line, 51 quasars; and 1.8–4.3= green short long dashed line, 49 quasars). The red solid line show the bolometric correction for E94 RQ mean SED. The red star point at B band (4400\AA) show the bolometric correction calculate from the Hopkins et al. (2007), assuming $\log L_{bol} = 45.5 \text{ erg/s}$, which is the median L_{bol} of SSRQ200. The red square show the bolometric correction at 3000\AA and 5100\AA respectively from Runnoe et al. (2012). In the bottom panel we show the dispersion of the bolometric correction for the SSRQ200 sample.

As mentioned above L_{bol} might overestimate the quasar emission for two reasons, meanwhile L_{bol} might also underestimate the total emission for three reasons: (1) excluding the far-IR to radio emission; (2) excluding the hard X-ray emission, where we do not have data; (3) ignoring the reddening of the primary emission in the optical/UV. Therefore, in this paper, we necessarily use L_{bol} as an estimate of the emission from everything associated with quasar hereafter, including emission from the primary radiation as well as the radiation reprocessing of the primary emission.

To investigate the contribution to L_{bol} by different wavelength ranges, we calculated L_{ir} by integrating from $24\mu\text{m}$ to $1\mu\text{m}$, L_{opt} from $1\mu\text{m}$ to 912\AA and L_X from 0.5 keV to 40 keV. The fractions of the luminosity in different wavelength ranges are reported in Table 1 (The full table is available on line). Table 2 shows the median values and the ranges for L_{bol} , the fractions in three wavelength ranges, and the median values and the ranges for M_{BH} and Eddington ratio (which will be discussed in § 2.3). In general, the IR component ($1 - 24\mu\text{m}$) provides an equal or greater contribution compared to the optical/UV ‘big blue bump’ component ($0.1 - 1\mu\text{m}$).

Table 3. Bolometric Corrections for the SSRQ200 sample ¹

log λ (μm)	log ν (Hz)	All z		0.1 < z < 1.2		1.2 < z < 1.5		1.5 < z < 1.8		1.8 < z < 4.3	
		BC	σ	BC	σ	BC	σ	BC	σ	BC	σ
1.0	13.5	9.78	5.37	9.89	4.61	9.81	5.82	8.60	3.97	10.86	6.63
0.9	13.6	9.20	4.40	10.14	4.45	9.65	4.53	8.18	3.33	8.85	5.01
0.8	13.7	9.25	4.05	10.53	4.54	9.64	3.92	8.39	3.03	8.44	4.27
0.7	13.8	9.39	3.90	10.62	4.49	9.74	3.69	8.67	2.93	8.53	4.10
0.6	13.9	9.55	3.72	10.23	3.84	10.03	3.76	9.10	3.19	8.83	3.97
0.5	14.0	9.32	3.53	9.27	3.50	9.38	3.19	9.42	3.55	9.21	3.93
0.4	14.1	8.66	3.09	8.75	3.38	8.59	2.82	8.15	2.22	9.18	3.76
0.3	14.2	8.95	3.84	9.36	5.60	9.29	3.29	8.22	2.38	8.93	3.37
0.2	14.3	10.11	5.08	10.41	8.09	10.67	4.16	9.18	2.89	10.21	3.57
0.1	14.4	11.24	5.52	11.74	8.47	12.45	5.38	10.18	3.21	10.61	3.08
0.0	14.5	12.94	11.18	14.20	16.50	15.63	13.95	11.28	3.64	10.64	3.24
-0.1	14.6	12.42	16.46	15.82	31.83	12.37	6.52	10.75	3.17	10.72	4.13
-0.2	14.7	11.31	14.54	15.59	28.17	10.97	4.24	8.97	2.68	9.73	3.57
-0.3	14.8	9.91	5.62	11.98	9.37	10.50	3.70	8.56	2.58	8.59	3.44
-0.4	14.9	8.62	3.00	9.73	2.91	9.58	3.29	7.86	2.54	7.29	2.50
-0.5	15.0	8.13	4.25	9.77	5.23	8.96	4.59	7.41	3.46	6.35	2.38
-0.6	15.1	9.03	9.44	11.97	16.46	9.89	6.80	7.49	3.92	6.75	3.52
-0.7	15.2	9.64	11.98	13.63	19.77	10.65	11.24	7.74	4.51	6.51	3.77
-0.8	15.3	9.43	13.56	14.09	21.72	10.38	13.49	6.94	5.60	6.28	4.61
-0.9	15.4	10.17	14.21	14.62	23.45	10.84	13.06	8.11	5.96	7.08	5.38
-1.0	15.5	12.85	15.19	16.03	23.17	11.82	12.93	9.91	6.59	13.72	13.07

¹ After host galaxy subtraction.

2.2 Bolometric Correction

We then calculated the bolometric correction at various frequencies. The bolometric correction ($BC_\nu = L_{bol}/\nu L_\nu$) is the factor which transforms the luminosity in one band to the bolometric luminosity. As the host galaxy contribution is prominent for X-ray-selected quasars, we calculated the frequency-dependent BC in the rest frame 0.1–10 μm only for SSRQ200 after performing the host correction. The bolometric correction was calculated for a $\Delta \log \nu = 0.02$ grid. The bolometric luminosity used in the calculation is $L_{bol, hc}$, which is the integration of host-corrected SEDs, listed as the last column in Table 1.

The mean and dispersion of the BC_ν are listed in Table 3 and shown in Figure 1, where we also show the mean and dispersion of the BC_ν for quasars at different redshift bins. The mean BC_ν curves for different redshift bins are consistent with each other given the large dispersion at each wavelength (Figure 1). The dispersion is the largest at around 1 μm , where the host contribution is the highest and in the extreme UV part where quasar variability is likely to contribute significantly to the observed dispersion.

For comparison, we plot the E94 mean SED bolometric correction as red solid line in Figure 1. Hopkins et al. (2007) used a double power law to approximate the B band bolometric correction.

$$\frac{L_{bol}}{L_B} = 6.25 \left(\frac{L_{bol}}{10^{10} L_\odot} \right)^{-0.37} + 9.00 \left(\frac{L_{bol}}{10^{10} L_\odot} \right)^{-0.012}$$

To compare with the bolometric correction we got, we use the median value of L_{bol} ($10^{45.5}$ erg/s) in SSRQ200 to apply to the formula. The B band bolometric correction from Hopkins et al. (2007) is thus 9.99 (red star in Figure 1). More recently, Runnoe et al. (2012) study the SED of 63 bright quasars at low redshift and got linear bolometric correction of 4.2 ± 0.1 , 5.2 ± 0.2 and 8.1 ± 0.4 at 1450, 3000 and 5100 Å,

respectively (red square in Figure 1). These results generally agree with bolometric correction got from SSRQ200. Note that the X-ray-selected SSRQ200 generally do not have prominent ‘big-blue-bump’ as the optical-selected E94 or Runnoe et al. (2012) sample, thus the bolometric correction in the optical part is generally larger than the Runnoe et al. (2012) number.

2.3 Eddington Ratio

For SS200, the accretion rate relative to the Eddington rate (the Eddington ratio, λ_E) can be calculated given the bolometric luminosities derived in § 2.1, i.e.

$$\lambda_E = \frac{L_{bol}}{L_{Edd}} = \frac{L_{bol}}{\frac{4\pi G c m_p}{\sigma_e} M_{BH}} = \frac{L_{bol}}{1.26 \times 10^{38} (M_{BH}/M_\odot)}$$

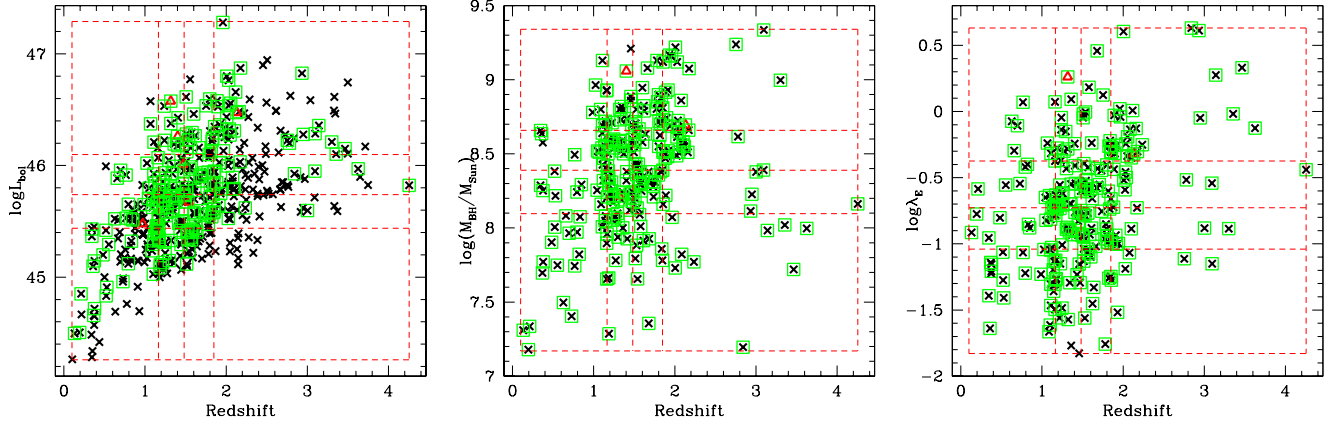
The black hole mass (M_{BH}) and the corresponding logarithm of the Eddington ratio ($\log \lambda_E$) of the XC413 are listed in Table 1 (Full table available on-line). The median and ranges of these parameters are reported in Table 2.

2.4 Parameter Space Classification

The XCRQ407 sample spans a wide range of z , L_{bol} , M_{BH} and λ_E (Table 2, Figure 2). The redshift range is comparable to that of Spitzer-SDSS sample (Richards et al. 2006), and the luminosity, black hole mass and Eddington ratio ranges are comparable to that of PG quasars (Sikora et al. 2007). The size of the XCRQ407 sample is more than double that of previous samples, and is an order of magnitude larger than the E94 sample. This large sample size spanning a wide range of the parameter spaces is useful to understand where and how the properties of the SMBH affect the SED shape.

Table 4. Parameter Space Bins

bin	redshift	N		L_{bol}	N		M_{BH}	N		$\log\lambda_E$	N
		XCRQ407	SSRQ200		XCRQ407	SSRQ200		SSRQ200	SSRQ200		SSRQ200
1	0.103–1.166	107	50	44.26–45.44	125	50	7.18–8.10	50		-1.828– -1.040	50
2	1.166–1.483	72	50	45.44–45.74	95	50	8.10–8.39	50		-1.040– -0.728	50
3	1.483–1.848	84	51	45.74–46.10	103	50	8.39–8.66	50		-0.728– -0.375	50
4	1.848–4.256	144	49	46.10–47.29	84	50	8.66–9.34	50		-0.375– 0.631	50

**Figure 2.** The classification of z , L_{bol} , M_{BH} and $\log\lambda_E$ bins of the XMM-COSMOS type 1 AGN sample. The dashed lines show the borders of quartile bins: the z bins (0.1 \sim 1.2 \sim 1.5 \sim 1.8 \sim 4.3), L_{bol} bins (44.3 \sim 45.4 \sim 45.7 \sim 46.1 \sim 47.3), M_{BH} bins (7.2 \sim 8.1 \sim 8.4 \sim 8.7 \sim 9.4) and $\log\lambda_E$ bins (-1.8 \sim -1.0 \sim -0.7 \sim -0.4 \sim 0.6). The black crosses show all the radio-quiet XMM-COSMOS type 1 AGN. The red triangles show the 6 radio-loud quasars. The green squares show the sub-sample SSRQ203.

We must note that XCRQ407 is an X-ray-selected sample, and also includes sources with large host galaxy contribution (Paper I). For this reason, we focus on the host-corrected SEDs of the SSRQ200. For comparison we also study the SEDs of the XCRQ407 before the host correction. The median values and ranges in z , L_{bol} , M_{BH} and $\log\lambda_E$ are similar for the two sub-samples (Table 2).

We can now check the SED shape dependence on each physical parameter by dividing the samples into quartiles of quasar z , L_{bol} , M_{BH} and λ_E , as shown by the dashed red lines in Figure 2. The bin boundaries and number of sources in different bins are given in Table 4. With these divisions, different bins have a similar number of quasars to calculate the mean SED, and therefore the possible statistical differences between different bins are minimized.

3 MEAN QUASAR SED DEPENDENCY ON PHYSICAL PARAMETERS

We can look for trends in the SEDs by checking the mean SED shape diversity in different bins. For each of the z , L_{bol} , M_{BH} and $\log\lambda_E$ bins the mean SED are calculated as in Paper I. Briefly we: (1). converted the flux densities at each frequency for each object to luminosity, using a Λ CDM Concordance Cosmology (Komatsu et al. 2009); (2). shifted them to the rest frame for each source; (3). corrected for the small Galactic extinction ($E(B-V) \simeq 0.017$); (4). limited the variability by restricting the photometry data in use to 2004 - 2007; (5). corrected for broad emission line contributions, which can be significant in the intermediate width

Subaru bands; (6). linearly interpolated the SED to a uniform frequency grid ($\Delta \log \nu = 0.02$); (7). calculated the mean SED at each $\log \nu$ grid point. To avoid the SED shape being dominated by the few luminous quasars in each bin, we also calculated the mean of the SED after normalizing the SED at $1\mu m$.

The resulting mean SEDs in different z and L_{bol} bins for XCRQ407 are shown in Figure 3. For ease of comparison, we also plot the E94 mean SED and a galaxy template from SWIRE (Polletta et al. 2007) normalized to the value of L_* from the UKIDSS Ultra Deep Survey (Cirasuolo et al. 2007, $M_K^* = -23$). The galaxy SED shown is an Elliptical galaxy with an age of 5 Gyr (E5 hereafter). Different galaxy templates have similar shapes at around $1\mu m$, so here we just choose E5 as a representative case.

The SEDs in our sample have much less pronounced $1\mu m$ inflection point than in E94. In Paper I we concluded that this shape is probably due to the host galaxy contribution. It is clear from Figure 3 that for low z and low L_{bol} sources the galaxy component around $1\mu m$ strongly affects the shape of the SEDs. Indeed at higher z and L_{bol} , the $1\mu m$ inflection becomes more obvious, as the quasar component becomes relatively stronger. However, even for high z and L_{bol} sources, the optical big blue bump is not as strong as in E94. This is probably because E94 considered a UV selected sample which picks out the bluest quasars. The mean SED shapes in the central z and L_{bol} bins are quite similar to the mean SEDs of all the quasars in XCRQ407.

For the SSRQ200 sample, we calculate the mean host-corrected SED for each bin, as shown in Figure 4. Even with

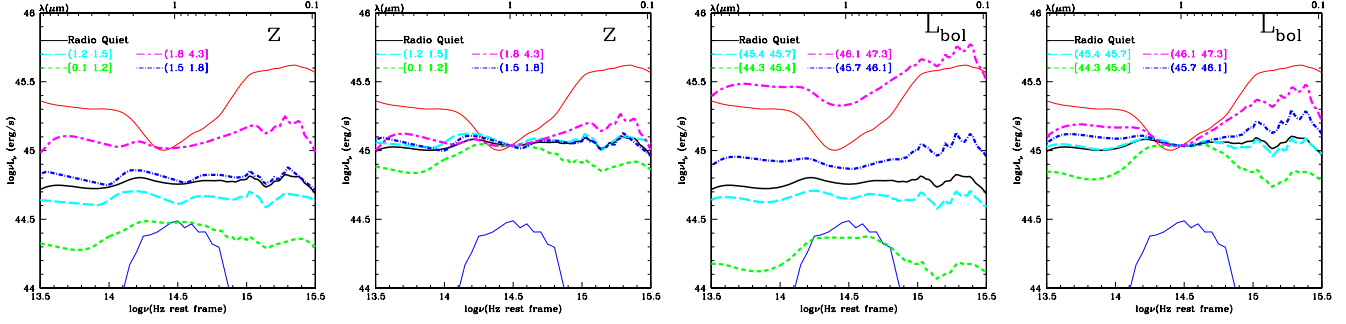


Figure 3. The mean SED for XCRQ407 in bins of z , L_{bol} before and after normalization at $1\mu m$ compared to E94 mean radio-quiet SED (red solid line). The black lines show the mean SED for all the radio-quiet type 1 AGN in the XMM-COSMOS sample. A host galaxy template (an Elliptical (5 Gyr), E5, blue solid line) is normalized to L_* from UKIDSS Ultra Deep Survey (Cirasuolo et al. 2007).

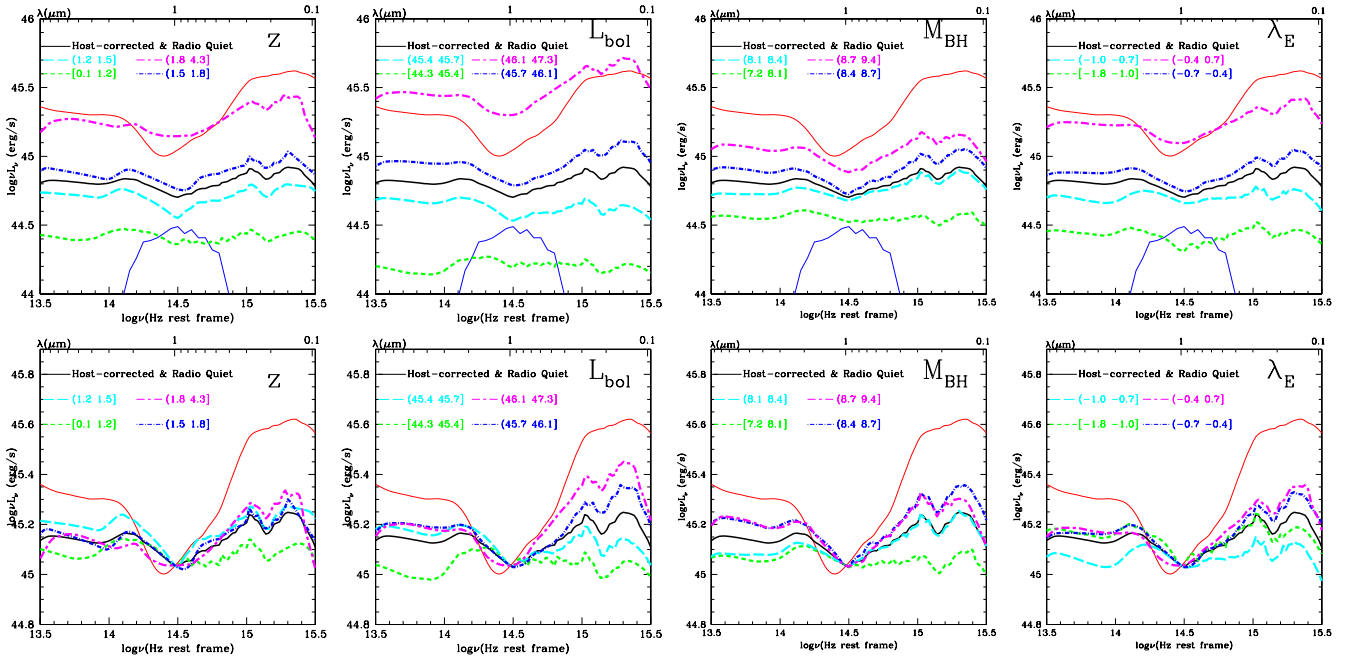


Figure 4. The host-corrected mean SED for SSRQ200 in bins of z , L_{bol} , M_{BH} and λ_E compared to E94 mean radio-quiet SED (red solid line): *top*: before normalization; *bottom*: normalized at $1\mu m$. The black solid lines show the host-corrected mean SED of all quasars in SSRQ200. A host galaxy template (an Elliptical (5 Gyr), blue solid line) is normalized to L_* from UKIDSS Ultra Deep Survey (Cirasuolo et al. 2007). Note that, to show the difference of the mean SEDs in different bins clearly, we expanded the y axis in all the plots of the bottom panel.

the host-correction, the mean SEDs for the low z , L_{bol} and M_{BH} sources are still relatively flat and different from E94. This may be due to insufficient host galaxy correction in some cases because of the scatter in the scaling relationship. The mean SEDs show that the top three bins of z , L_{bol} and M_{BH} have similar shapes, showing no sign of dependency on any of these parameters. The $1\mu m$ -normalized mean SED shapes of three $\log \lambda_E$ bins are also similar to each other except for the penultimate bin ($-1.0 < \log \lambda_E < -0.7$). The z bins have the tightest distribution compared to other parameters (e.g., at $3\mu m$ and 3000\AA the difference of the mean SEDs in different bins is 0.1 dex and 0.15 dex respectively, smaller than corresponding values of the other parameters). The difference of the mean SEDs in bins of each parameter are less than a factor of 2 even at the infrared/UV end.

To check for partial dependencies of the SED shape on

the physical parameters, we checked the SED shape difference with one parameter when fixing another. In order to have a large enough number of quasars in the mean SED calculation in each sub-bin, we consider the central two bins (Figure 5). The number of quasars in each sub-bin is listed in Table 5. As the number of quasars in each sub-bin is relatively small, these mean SEDs are more affected by particular SED shapes. In all these plots, the bottom / first bins are still affected by the host contribution, and the top / last bins are sometimes affected strongly by several specific SEDs (e.g. hot-dust-poor quasars, Hao et al. 2010, 2011). However, in general, the mean SEDs shapes in different sub-bins are very similar to each other and to the mean SED in that bin. For instance, when fixing z , the top / last two L_{bol} sub-bins have a similar mean SED shape, while the mean SED

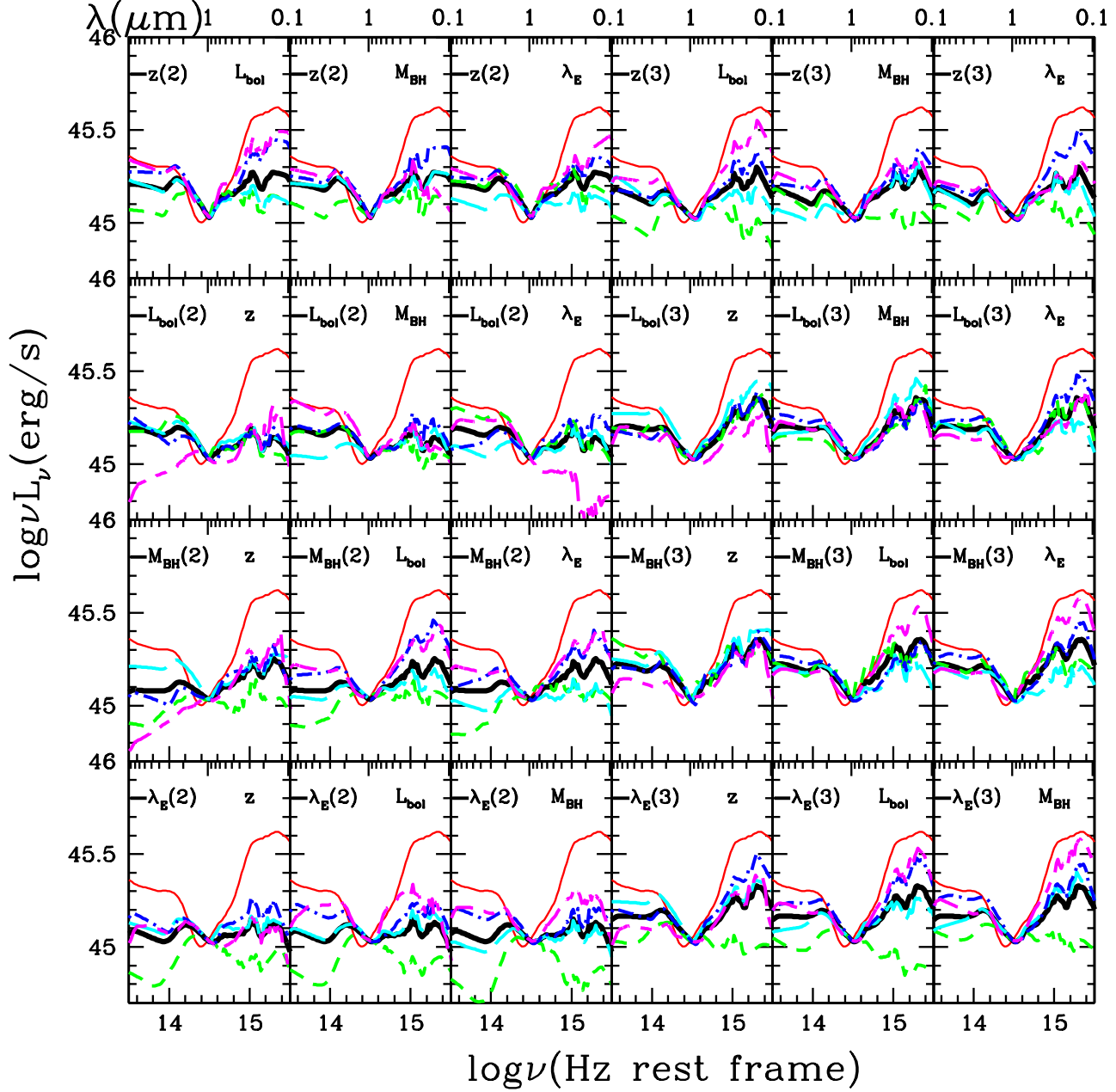


Figure 5. The mean host-subtracted SED normalized at $1\mu\text{m}$ compared to E94 mean radio-quiet SED (red solid line). Different rows are for quasars in specific bins: (1) z bin 2 (left half $1.2 < z < 1.5$) and bin 3 (right half, $1.5 < z < 1.8$); (2) $\log L_{\text{bol}}$ bin 2 (left half $45.4 < \log L_{\text{bol}} < 45.7$) and bin 3 (right half, $45.7 < \log L_{\text{bol}} < 46.1$); (3) $\log(M_{\text{BH}}/M_{\odot})$ bin 2 (left half $8.1 < \log(M_{\text{BH}}/M_{\odot}) < 8.4$) and bin 3 (right half, $8.4 < \log(M_{\text{BH}}/M_{\odot}) < 8.7$); (4) $\log \lambda_E$ bin 2 (left half $-1.0 < \log \lambda_E < -0.7$) and bin 3 (right half, $-0.7 < \log \lambda_E < -0.4$). The symbol on the upper right corner of the each plot shows which sub-bin is considered. The lines are color coded as in Figure 4.

shapes in different M_{BH} or $\log \lambda_E$ bins show no significant difference.

The lack of SED shape dependency on z , L_{bol} , M_{BH} and λ_E we observed in the XCRQ407 and SSRQ200 suggests that neither the emission mechanism nor the accretion disk and ‘torus’ structure alters systematically or dramatically with these parameters. In other words, a single intrinsic quasar SED in the optical/UV to near-infrared range is a meaningful concept.

4 SED DISPERSION DEPENDENCY ON PHYSICAL PARAMETERS

Even if the mean SEDs show little or no dependency on physical parameters, the SED dispersion may change with them. We checked the SED dispersion in different bins for both the XCRQ407 and SSRQ200. In order to exclude the dispersion caused by different brightness of quasars and concentrate on the SED shape dispersion, we only consider the

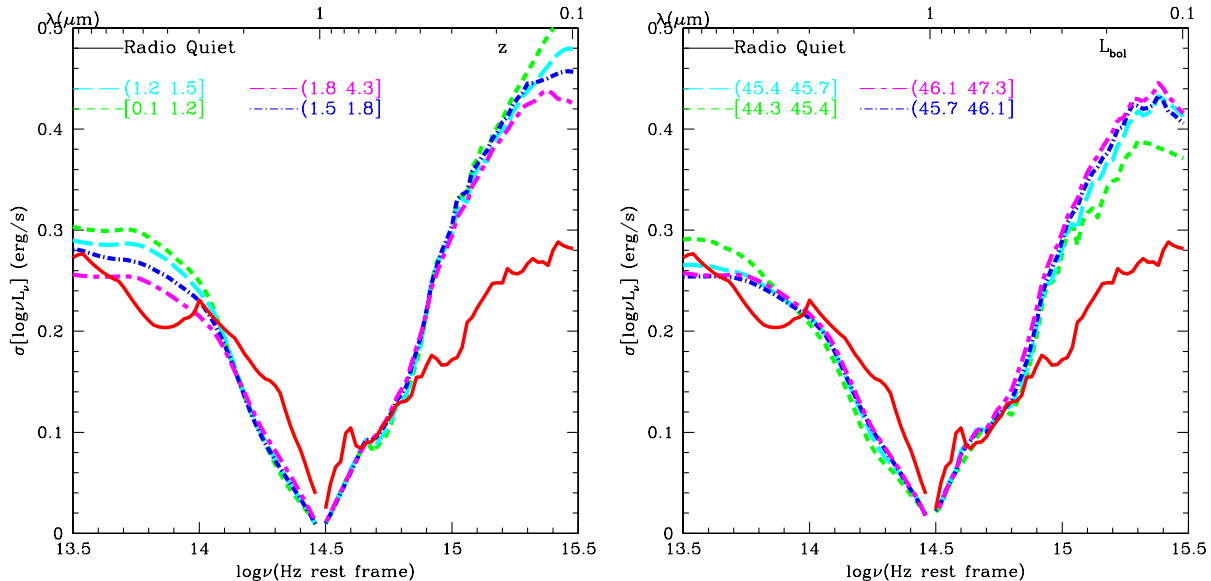


Figure 6. The dispersion of the SEDs for XCRQ407 in bins of z and L_{bol} after normalization at $1\mu m$ compared to E94 radio-quiet SED dispersion (red solid curve).

dispersion of the SEDs after normalizing all the SEDs at $1\mu m$. The SED dispersion in different bins at certain specific wavelengths are listed as examples in Table 6.

The resulting dispersion of normalized SEDs in z and L_{bol} bins for XCRQ407 compared to E94 radio-quiet SED dispersion are shown in Figure 6. The XMM-COSMOS SEDs generally have a larger dispersion in the optical to UV range compared to E94 radio-quiet sample. This is probably because E94 is biased toward blue quasars, unlike the XMM selected XCRQ407, thus it does not include quasars with various optical shapes/colors. The $1-10\mu m$ dispersion of XCRQ407 is closely similar to E94, except at $\sim 2\mu m$, where it is somewhat lower. The XMM-COSMOS SED dispersion is almost exactly the same in the $3\mu m$ to 3000 \AA range for different z or L_{bol} bins. The SED dispersions in this range are all below a factor of 2.

For the host-corrected SSRQ200 sample, the dispersion of the SED for each bin is shown in Figure 7. We can see that the dispersion in different M_{BH} bins has most similarity between bins compared to other parameters (z , L_{bol} and $\log \lambda_E$). The SED dispersion in the $3\mu m$ to 3000 \AA range is not as tight as the un-corrected sample, implying extra dispersion induced by the host-correction process depend on z , L_{bol} or λ_E . The lowest bin for each parameter always has the largest dispersion. The $3-8\mu m$ dispersion is larger than E94 in the bottom one or two bins for all parameters.

In all these SED dispersion plots, the UV dispersion is generally larger than the near-IR dispersion. This could mean that the reprocessing or the hot dust component is more uniform than the accretion disk emission. Alternatively, this could be completely caused by the variability of the quasar which affects the UV SED most.

5 DISCUSSION AND CONCLUSION

We analyzed the dependence of both the mean and dispersion of the SED shapes in the optical-UV to IR range on the parameters z , L_{bol} , M_{BH} and $\log \lambda_E$ for the 407 XMM-COSMOS radio-quiet type 1 AGN sample. We also calculated the bolometric correction at UV-optical to near-IR for the host-corrected SSRQ200, and in four different redshift bins.

As the XMM-COSMOS quasar sample is an X-ray-selected sample, it includes also sources with low nucleus to host contrast. The mean SED of the whole sample is greatly affected by the host galaxy emission for low redshifts and luminosities. Therefore, we mainly studied the mean and dispersion SEDs of a host-corrected sub-sample of 200 radio-quiet quasars, SSRQ200, in four quartile bins of z , L_{bol} , M_{BH} and λ_E . The mean SED shapes in the different bins are quite similar to each other. These SEDs are also generally similar to the E94-like mean SED shape, but they tend to have less pronounced optical to UV bump emission than in E94, as E94 is biased towards blue quasars. Even if we fix one parameter (e.g. redshift), the mean SEDs show no obvious evolution with the others.

We checked the dispersion of SEDs in different parameter bins. The near-IR SED dispersion is generally smaller compared to the UV SED dispersion, which might be due to the variability of the quasar that mainly affects UV SED. The SEDs before and after host correction have very similar dispersion in the $3\mu m$ to 3000 \AA range for different bins, which implies an invariant intrinsic dispersion of SED shapes in this wavelength range. However, in this wavelength range, the host-corrected SED dispersion is not as tight as the uncorrected sample, probably due to the extra dispersion induced by the scaling relationship depends on the physical parameters. The host-corrected SED dispersion in different M_{BH} bins has most similarity between bins compared to other parameters (z , L_{bol} and $\log \lambda_E$).

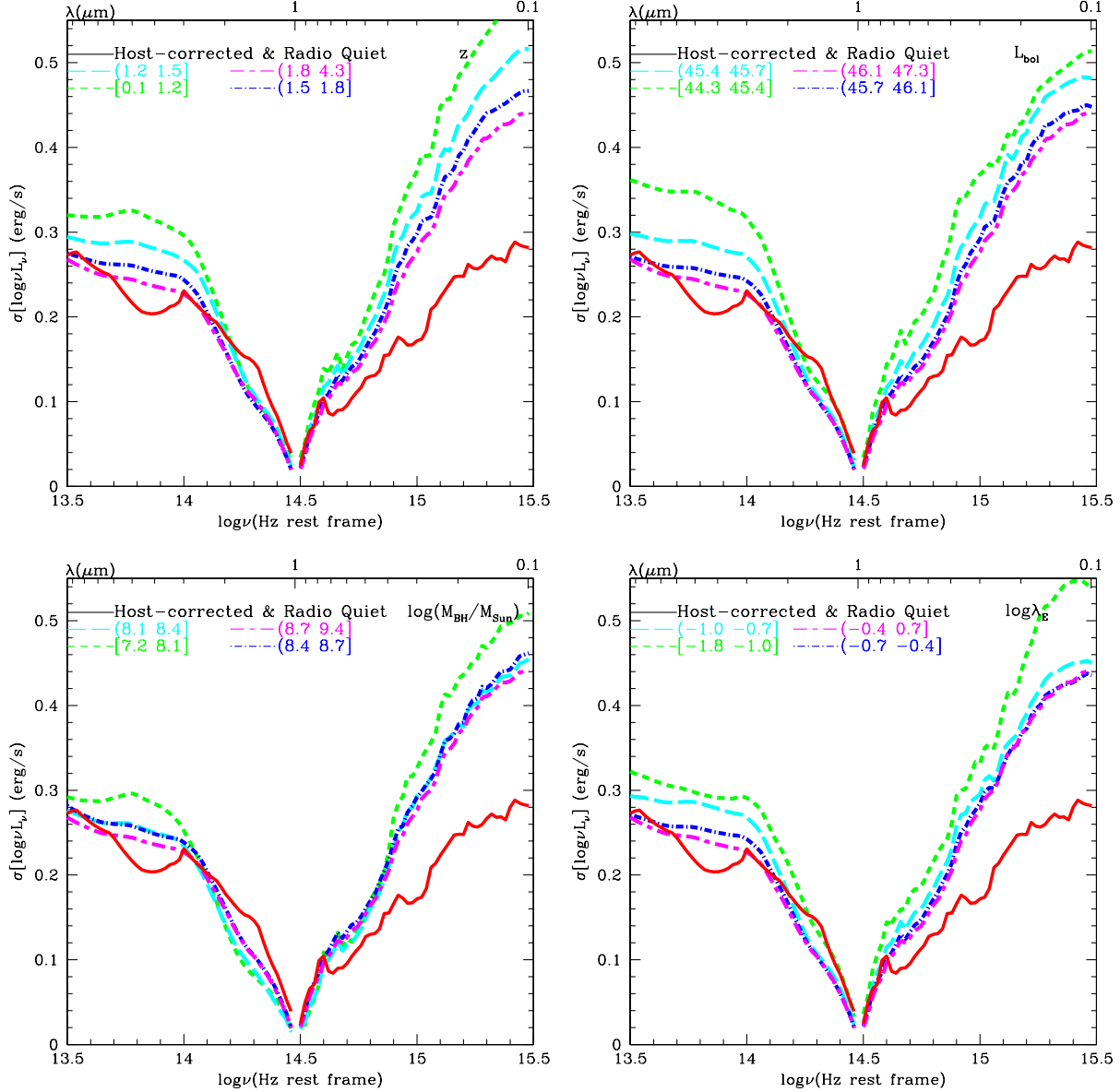


Figure 7. The dispersion of host-subtracted SEDs for SSRQ200 in bins of z , L_{bol} , M_{BH} and λ_E after normalized at $1\mu m$ compared to E94 radio-quiet SED dispersion (red solid curve).

There is no obvious sign of dependency of the mean SED with z , L_{bol} , M_{BH} or $\log \lambda_E$. This result implies that the global quasar structures (the accretion disk and the ‘torus’) are invariant with respect to these parameters. Despite the strong expectation that feeding of the AGN and host galaxy is likely to change (e.g. Merloni et al 2010), as well as the X-ray corona is likely to change (α_{OX} varies with λ_E , e.g. Lusso et al. 2010), the accretion disk and the ‘torus’ seem to not depend on this mechanism. Thus an intrinsic SED in UV-optical to near-IR exists.

The differences among the SEDs show there might be diversity only at the second order. Host contamination, reddening and quasar variability should lead to a dispersion in the UV and near-IR SEDs. The lack of SED dispersion evolution indicates that these effects themselves do not show much systematic dependence on physical parameters.

All the above conclusions depend on the reliability of the host correction process. This assumes the scaling relationship between black hole mass and bulge mass (e.g. Marconi & Hunt 2003) with an evolutionary term (Bennert et al. 2010, 2011). Uncertainties in this correlation might limit our ability to detect SED shape dependency on physical parameters.

A less model dependent analysis will be described in a following paper (Hao et al. 2012b), where we introduce a new mixing diagram to readily distinguish different SED shape, i.e. galaxy-dominated, quasar-dominated and reddening dominated SEDs.

So far, we have only studied the SED shape one decade on either side of $1\mu m$. To study the SED shape evolution in UV or FIR is less easy. The UV is greatly affected by both reddening and variability that is different for different

Table 5. Number of SSRQ200 quasars in Sub-bins for Partial Evolution

	bin		N in sub-bin		λ_E
	sub-bin	z	L_{bol}	M_{BH}	
$z(2)$	1		12	9	11
	2		18	19	14
	3		13	14	16
	4		7	8	9
$z(3)$	1		12	10	11
	2		13	16	16
	3		12	10	14
	4		14	15	10
$\log L_{bol}(2)$	1	14		11	16
	2	18		17	17
	3	13		11	12
	4	5		11	5
$\log L_{bol}(3)$	1	8		10	6
	2	13		11	15
	3	12		14	17
	4	17		15	12
$\log M_{BH}(2)$	1	9	13		8
	2	19	17		16
	3	16	11		15
	4	6	9		11
$\log M_{BH}(3)$	1	10	10		15
	2	14	11		12
	3	10	14		11
	4	16	15		12
$\log \lambda_E(2)$	1	11	14	9	
	2	14	17	16	
	3	16	15	12	
	4	9	4	13	
$\log \lambda_E(3)$	1	10	9	15	
	2	16	12	15	
	3	14	17	11	
	4	10	12	9	

sources. The FIR is greatly affected by host galaxy star formation, which also varies from case to case. We will discuss these two regions of the quasar SED in following papers.

ACKNOWLEDGMENTS

HH thanks Belinda Wilkes and Martin J. Ward for discussion. This work was supported in part by NASA *Chandra* grant number G07-8136A (HH, ME, FC) and the Smithsonian Scholarly Studies (FC). Support from the Italian Space Agency (ASI) under the contracts ASI-INAF I/088/06/0 and I/009/10/0 is acknowledged (AC and CV). MS acknowledges support by the German Deutsche Forschungsgemeinschaft, DFG Leibniz Prize (FKZ HA 1850/28-1).

REFERENCES

- Appleton, P. N., et al., 2004, ApJS, 154, 147
 Barth, A. J., Martini, P., Nelson, C. H., Ho, L. C. 2003, ApJL, 594, 95

Table 6. SED Dispersions at Certain Wavelength

bin		Wavelength				
sub-bin		10 μm	3 μm	3000 \AA	2500 \AA	1000 \AA
XCRQ407 z	1	0.30	0.25	0.30	0.36	0.50
	2	0.29	0.24	0.30	0.35	0.48
	3	0.28	0.23	0.30	0.36	0.46
	4	0.26	0.21	0.30	0.34	0.42
XCRQ407 $\log L_{bol}$	1	0.29	0.21	0.28	0.31	0.37
	2	0.27	0.21	0.28	0.32	0.41
	3	0.25	0.21	0.29	0.34	0.41
	4	0.26	0.22	0.30	0.35	0.42
SSRQ200 z	1	0.32	0.30	0.37	0.42	0.57
	2	0.29	0.27	0.32	0.36	0.52
	3	0.28	0.24	0.30	0.33	0.47
	4	0.27	0.23	0.28	0.31	0.44
SSRQ200 $\log L_{bol}$	1	0.36	0.32	0.37	0.39	0.51
	2	0.30	0.27	0.32	0.35	0.48
	3	0.27	0.24	0.29	0.33	0.45
	4	0.27	0.23	0.28	0.31	0.44
SSRQ200 $\log M_{BH}$	1	0.29	0.25	0.33	0.37	0.51
	2	0.28	0.23	0.29	0.33	0.45
	3	0.28	0.24	0.29	0.32	0.46
	4	0.27	0.23	0.28	0.31	0.44
SSRQ200 $\log \lambda_E$	1	0.32	0.29	0.33	0.37	0.54
	2	0.29	0.27	0.30	0.33	0.45
	3	0.27	0.24	0.28	0.31	0.44
	4	0.27	0.23	0.28	0.31	0.44

- Bennert, V. N., Treu, T., Woo, J.-H., Malkan, M. A., Le Bris, A., Auger, M. W., Gallagher, S., Blandford, R. D., 2010, ApJ, 708, 1507
 Bennert, V. N., Auger, M. W., Treu, T., Woo, J.-H., Malkan, M. A., 2011, ApJ, 742, 107
 Brandt, W. N., et al. 2002, ApJL, 569, 5
 Brusa, M. et al. 2009, ApJ, 693, 8
 Brusa, M., et al., 2010, ApJ, 716, 348
 Cappelluti, N., et al., 2007, ApJS, 172, 341
 Cappelluti, N., et al., 2009, A&A, 497, 635
 Cirasuolo, M. et al. 2007, MNRAS, 380, 585
 Civano, F., et al., 2011, ApJ, 741, 91
 Cowie, L. L., et al. 2003, ApJ, 584, L57
 Czerny, B., & Elvis, M., 1987, 321, 305
 Dunne, L. & Eales, S. A. 2001, MNRAS, 327, 697
 Elvis, M. et al., 1994, ApJS, 95, 1
 Elvis, M. et al., 2012, ApJ, accepted, astro-ph/1209.1478
 Ferrarese, L. & Merrit, D. 2000 ApJ, 539, L9
 Fiore, F. et al. 2003, A&A, 409, 79
 Gebhardt, K., et al., 2000, ApJ, 539, L13
 Goldschmidt, P., Kukula, M. J., Miller, L., & Dunlop, J. S., 1999, ApJ, 511, 612
 Haardt, F., & Maraschi, L. 1991, ApJ, 380, L51
 Hao, H., et al., 2010, ApJ, 724, L59
 Hao, H., et al., 2011, ApJ, 733, 108
 Hao, H., et al., 2012a, ApJL submitted
 Hao, H., et al., 2012b, MNRAS, submitted
 Harris, D. E., & Krawczynski, Henric, 2006, ARA&A, 44, 463
 Hasinger, G., et al., 2007, ApJS, 172, 29

- Ho, L. C., 1999, ApJ, 516, 672
 Ho, L. C., 2005, ApJ, 629, 680
 Ho, L. C., 2007, ApJ, 669, 821
 Ho, L. C., 2008, ARA&A, 46, 475
 Hopkins, P., Richards, G. T., & Hernquist, L., 2007, ApJ, 654, 731
 Jiang, L. et al., 2006, AJ, 132, 2127
 Jiang, L., Fan, X., Vestergaard, M., Kurk, J. D., Walter, F., Kelly, B. C., & Strauss, M. A., 2007, AJ, 134, 1150
 Just, D. W., Brandt, W. N. et al., 2007, ApJ, 665, 1004
 Kawaguchi, T., Shimura, T., & Mineshige, S. 2001, ApJ, 546, 966
 Komatsu, E., et al., 2009, ApJS, 180, 330
 Kormendy, J. & Richstone, D. 1995, ARA&A, 33, 581
 Kurk, J. D. et al. 2007, ApJ, 669, 32
 Laor, A., Netzer, H., & Piran, T. 1990, MNRAS, 242, 560
 Lapi, A. et al. 2011, ApJ, 742, 24
 Lilly, S. J., et al., 2007, ApJS 172, 70
 Lilly, S. J., et al., 2009, ApJS 184, 218
 Lusso, E., et al., 2010, A&A 512, 34
 Magorrian, J., et al., 1998, AJ, 115, 2285
 Mainieri, V., et al., 2007, ApJS, 172, 368
 Marconi, A. & Hunt, L. K. 2003, ApJ 589, L21
 Mateos, et al. 2005, A&A, 433, 855
 Mathur, S., Wilkes, B. J. & Ghosh, H. 2002, ApJL, 570, 5
 McAlary, C. W. & Rieke, G. H. 1988, ApJ, 333, 1
 McLure, R. J. & Jarvis, M. J., 2002, MNRAS, 337, 109
 Menci, N., et al. 2008, ApJ, 686, 219
 Merloni, A., et al. 2010, ApJ 708, 137
 Mortlock, D. J., et al., 2011, Nature, 474, 616
 Mullaney, J. R., et al. 2012, MNRAS, 419, 95
 Netzer, H. et al. 2007 ApJ, 666, 806
 Peng, C. Y., Impey, C. D., Rix, H.-W., Kochanek, C. S., Keeton, C. R., Falco, E. E., Lehár, J., McLeod, B. A. 2006, ApJ, 649, 616
 Polletta, M. et al. 2007, ApJ, 663, 81
 Rees, M.J. 1984, ARA&A, 22, 471
 Richards, G. T. et al. 2006, ApJS, 166, 470
 Richstone, D., et al. 1998, Nature, 395, 14
 Runnoe, J. C., Brotherton, M. S., Shang, Z., et al., 2012, MNRAS, 422, 478
 Sanders, D. B., Phinney, E. S., Neugebauer, G., Soifer, B. T., & Matthews, K. 1989, ApJ, 347, 29
 Schneider, D. P. et al. 2007, AJ, 134, 102
 Scoville, N. Z., et al., 2007, ApJS, 172, 1
 Shakura, N. I., & Sunyaev, R. A., 1973, A&A, 24, 337
 Sikora, M., Stawarz, L. & Lasota, J. P., 2007, ApJ, 658, 815
 Silverman, J. D. et al. 2002, ApJL, 569, 1
 Silverman, J. D. et al. 2005, ApJ, 624, 630
 Shields, G. A., Menezes, K. L., Massart, C. A., Vanden Bout, P. 2006, ApJ, 641, 683
 Steffen, A. T., Strateva, I., et al., 2006, AJ, 131, 2826
 Steinhardt, C. L. & Elvis, M. 2010, MNRAS, 402, 2637
 Stocke, J. T., Morris, S. L., Weymann, R. J. & Foltz, C. B., 1992, ApJ, 396, 487
 Suganuma, M. et al. 2006, ApJ, 639, 46
 Terashima, Y. & Wilson, A. S. 2003, ApJ, 583, 145
 Tremaine, S., et al. 2002, ApJ, 574, 740
 Trump, J.R. et al. 2009a ApJ, 696, 1195
 Trump, J.R. et al. 2009b ApJ, 700, 49
 Ueda, Y. et al. 2003 ApJ 598, 886
 Vestergaard, M. 2004, ApJ, 601, 676
 Vestergaard, M. & Peterson, B. M. 2006 ApJ 641, 689
 Vignali, C., Brandt, W. N., Schneider, D. P. 2003a, AJ, 125, 433
 Vignali, C. et al. 2003b, AJ, 125, 2876
 Wilkes, B. J., 2003, ASPC, 311, 37
 Wilkes, B. J. & Elvis, M., 1987, ApJ, 323, 243
 Williams, O. R., et al., 1992, ApJ, 389, 157
 Young, M., Elvis, M., Risaliti, G., 2010, AJ, 708, 1388
 Zamorani, G., Henry, J.P., Maccacaro, T., et al. 1981, ApJ, 245, 357
 Zdziarski, A. A., Poutanen, J., & Johnson, W. N. 2000, ApJ, 542, 703